

Enabling pure CO₂ reduction on Ni-YSZ electrodes: Operando studies indicate an oxide-mediated mechanism

Vipin Kamboj, Soham Raychowdhury, Chinmoy Ranjan*

Department of Inorganic and Physical Chemistry, Indian Institute of Science, Bengaluru 560012

ranjan@iisc.ac.in

Abstract

Ni-YSZ-based electrodes are well-established in the field of solid oxide technologies. Ni/YSZ-based architectures have well-known performance and mechanical properties besides well-established manufacturing processes. Solid oxide-based CO₂ electrolysis on Ni-YSZ at high temperature requires the presence of H₂ in the CO₂ inlet stream. It is believed that in pure CO₂ streams the reaction fails due to oxidation of the Ni-YSZ electrode. Using operando Raman spectroscopy and online mass spectroscopy, we have shown that CO₂ can in fact be reduced on the Ni-YSZ surface. Our measurements, reveal that Ni-YSZ oxidizes to NiO_x-YSZ within a pure CO₂ stream. CO₂ electrolysis is possible on this oxide surface via a surface oxygen and vacancy-mediated mechanism similar to those observed within other oxide cathodes such as CeO_x. The deactivation of the electrode coincides with strongly reducing conditions and at current densities > 400 mA/cm², NiO_x is completely reduced coinciding with complete stoppage of CO production. Cu-impregnation into Ni-YSZ was demonstrated to mitigate the deactivation issue by forming a more stable surface oxide on Ni which continued to carry out CO₂ reduction under strongly reducing conditions. The new electrode demonstrated improved kinetics and stability against carbon deposition via Boudouard reaction.

Introduction

Global targets of CO₂ reduction require aggressive mitigation of CO₂ production and increased capture.¹ Capturing CO₂ from various sources (including air) and converting it into synthetic fuel using green energy is an excellent way of making the fuel usage cycle carbon neutral.²⁻⁴

High-temperature electrochemical reduction of CO₂ within a solid oxide electrolysis cell (SOEC) is an attractive approach allowing for cost-effective and energy-efficient production of CO.^{5,6} The electrochemical conversion of CO₂ to CO is relatively energy efficient with 100% faradaic efficiency and greater than 90% energy efficiency. The efficiency losses increase significantly when higher hydrocarbons are targeted. Creation of heavily reduced products such as CH₄, requires multiple electron and proton transfer steps (8e⁻ and 8H⁺). Such multistep electrochemical reactions result in high energy losses owing to slower kinetics. CO production from CO₂ is a 4e⁻ process and thus kinetically easier. Ideally, CO produced from renewable electricity can be easily coupled with the well-known Fischer Tropsch process resulting in energy-efficient production of higher synthetic hydrocarbons (**Figure 1**).^{7,8} SOECs have the advantages of excellent kinetics along with selectivity towards the products and they are more electrical energy-efficient due to the high operating temperature (~ 800 °C) which reduces cell voltage.⁹⁻¹¹

CO₂ electrolysis using Solid Oxide Electrolyzers

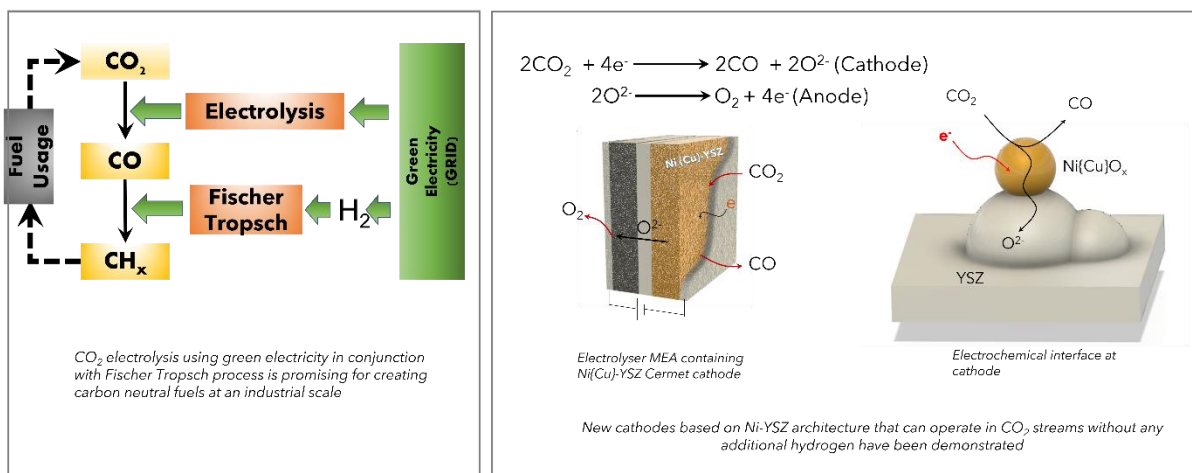


Figure 1: *CO₂ neutral fuel cycle. Green electricity can be channelled into energetic fuels using a combination of CO₂ electrolysis and Fischer Tropsch Reaction. This study has demonstrated the CO₂ electrolysis without using additional H₂ with copper-impregnated Ni{Cu}_x-YSZ electrodes.*

CO₂ electrolysis is carried out on a membrane electrode assembly comprising of a CO₂-reducing cathode, a solid oxide electrolyte, and an oxygen-evolving anode. Nickel on yttria-stabilized zirconia cermet (Ni-YSZ) serves as the popular choice for the cathode. Perovskites such as (La_{0.8}Sr_{0.2})_{0.95}MnO_{3-x} (LSM-YSZ) and YSZ serve as popular choices for oxygen-evolving anode and electrolyte respectively.^{6,12-17}

Besides Ni-YSZ, several electrode materials have been tested as cathodes. These include perovskites such as La_{0.35}Sr_{0.65}TiO_{3-x}, Sr₂FeMo_{0.5}O_{6-x}, (La_{0.75}Sr_{0.25})_{0.95}Cr_{0.5}Mn_{0.5}O_{3-x}, La_{0.2}Sr_{0.8}TiO_{3-x}, La_{0.75}Sr_{0.25}Cr_{0.5}Mn_{0.5}O_{3-x} and CeO_{2-x}.^{11,18-28} They have the advantage over Ni-YSZ in terms of high ionic and electronic conductivity, better redox stability, and resistance to carbon deposition and sulphur poisoning. However, the poor catalytic activity of perovskites compared to Ni-YSZ makes the latter a preferred material.²⁹⁻³¹ Due to its popularity as a SOFC anode, Ni-YSZ has been well-studied and known in the industry. Well-established manufacturing processes leverage its good electrical, catalytic, and mechanical characteristics to create efficient membrane electrode assembly (MEA) architectures. Anode-supported SOFC based on Ni-YSZ are well known for mechanical stability and high efficiency in fuel cells as they enable very thin electrolyte layers. Ni-YSZ is a well-established anode for the SOFC-H₂ fuel cell.^{32,33} But when it comes to CO₂ electrolysis, several challenges remain.³⁴ In a pure CO₂ atmosphere, the Ni-YSZ electrode is believed to degrade by oxidizing into NiO_x.³⁵ This results in catastrophic deactivation of the electrode and even cell failure. Feeding CO along with CO₂ can mitigate this problem to some extent. However, Ni remains a good catalyst for carbon deposition via the Boudouard reaction {2CO → C + CO₂}, resulting in another pathway for electrode deactivation.^{6,18,37} This challenge is avoided by using Ni/YSZ electrodes along with a small percentage of H₂ at the inlet of the reaction chamber. The hydrogen maintains a reducing atmosphere at the electrode allowing for sustained CO production. The introduction of H₂ into the reactant stream introduces additional complexity. It not only creates dependency issues on H₂ delivery infrastructure (rather lack of it), but

the presence of H₂ at the cathode also enables thermochemical reverse water gas shift (RWGS) reaction.³⁹⁻⁴¹ A cathode catalyst that can directly convert a pure CO₂ stream into CO with a sustained performance would be of value.

We believe that rather than starting from scratch, there is merit in altering the existing Ni-YSZ based cathode architecture to achieve our electrocatalytic goals. It can reduce the significant time and effort involved in translation to large-scale devices as it can leverage the current manufacturing and process supply chains.

Pure CO₂ electrolysis has been a subject of interest. Xie and Coworkers have studied Ni-based catalyst for pure CO₂ electrolysis. Specifically, they have indicated improved performance on electrodes such as Ni/Cr₂O_{3-x}.⁴² Ye et al. have reported CO₂ electrolysis on (La, Sr)TiO_{3-x} cathodes and have shown that “carbonate type” species can form upon CO₂ adsorption on the cathode using in situ infrared spectroscopy in combination with temperature programmed desorption experiments.^{17,43} Wang et al. have shown that electrodes that result in in-situ exsolution of nanoscale metal/metal oxide interfaces perform well in CO₂ reduction.⁴⁴

In this manuscript, we have shown that altering the Ni-YSZ electrode by infiltration of Cu-containing salt can achieve high and sustained electro-reduction performance within a pure CO₂ stream. Using online mass spectrometry and operando Raman spectroscopy, we have characterized the cathode performance of pure Ni-YSZ, and its Cu infiltrated counterpart (Ni{Cu}_x-YSZ) by simultaneously tracking catalyst structure and product formation within reaction streams. The pretreatment steps leading to active catalyst formation have also been characterized. Our results, for the first time, allow a direct spectroscopic evaluation of the Ni-YSZ catalyst deactivation process and its mitigation within the Cu-infiltrated counterpart. We have shown that within the Ni-YSZ catalyst, the active material for CO₂ reduction is a type of nickel oxide (NiO_x) which easily develops under open circuit conditions in the presence of CO₂. We have argued that CO₂ reduction on the active catalyst material NiO_x follows an oxide-mediated mechanism where surface oxygen and vacancies mediate a carbonate-type intermediate as proposed in LSM and CeO_{2-x} type cathodes. We have proposed that the active material

is likely to be a dynamically stable oxide that has sufficient vacancies and stability to interact with the CO₂ molecule and transfer the O²⁻ ion to the electrolyte. We have shown that a progressive regime of cathodic current application results in the complete removal of the oxide layer and, consequently catalyst deactivation. The Cu infiltrated catalyst on the other hand allows the formation of a “stable” oxide layer that can engage with CO₂ molecule and reduce it to CO. We have shown that Ni{Cu}_x-YSZ catalyst also suppresses the Boudouard reaction. Our results indicate that it’s possible to develop new catalysts for pure CO₂ reduction by using earth-abundant metals such as Ni and Cu.

Preparation of the solid Membrane Electrode Assembly (MEA)

The solid MEA was prepared by screen printing NiO-YSZ (66:34) and LSM-YSZ (50:50) inks on the sides of YSZ solid electrolyte (220 μm thickness, 25 mm diameter) forming the cathode and anode respectively. All the above materials were obtained from Fuel Cell Materials. The MEA was air-dried at 30°C for 8 hours. Subsequently, it was heated (air, heating rate (2°C/min)) up to 1050°C and annealed for 3 hours. The cell was allowed to furnace cool to room temperature. For electrodes modified with Cu (Ni{Cu}-YSZ), a 20 μl precursor solution of 0.2 M CuNO₃ (Thomas Baker) was infiltrated into the NiO-YSZ electrode and dried at 30°C for 12 hrs to allow impregnation of precursor solution into the electrode. It was followed by sintering at 800°C for an hour. After furnace cooling, current collectors (porous Ag paste, Fuel Cell Materials) were screen printed on both sides of the pellet. The MEA was dried at 30°C for 6 hrs followed by sintering at 500°C for 1 hr (heating rate 5°C/min). All the measurements were carried out in a 3-electrode geometry with the concentric Ag reference electrode screen printed on the cathode side around the LSM-YSZ electrode as shown in **Figure S1**.

The electrode geometry used is similar to that suggested by Rutman et al. which averages out the effects of WE-CE misalignment for planar electrode geometries.⁴⁵ Thereafter, the cell was mounted on a stainless steel (SS) reactor. The gas flow was monitored using a mass flow controller. The cell outlet was connected to a mass spectrometer (Hiden HPR-40) for online gas analysis. Electrochemical studies were carried out using Autolab PGSTAT 30. Operando Raman studies were performed using InVia confocal Raman Microscope (Renishaw) using a 532 nm laser. For operando studies at high

temperature, a 2-chamber operando cell was constructed in-house. Further characterization details are provided in the supporting information (**Supplementary Note 1**).

Characterization of Electrodes

Materials were characterized using powder X-ray diffraction (PXRD), scanning electron microscopy (SEM, EDX), transmission electron microscopy (TEM), Raman spectroscopy (Renishaw), X-ray photoelectron spectroscopy (XPS), Auger electron spectroscopy (AES) and temperature programmed reactivity (TPR) studies were carried out using a customized TPR setup. Further details of the experimental setup are provided in the supporting information (**Supplementary Note 2**).

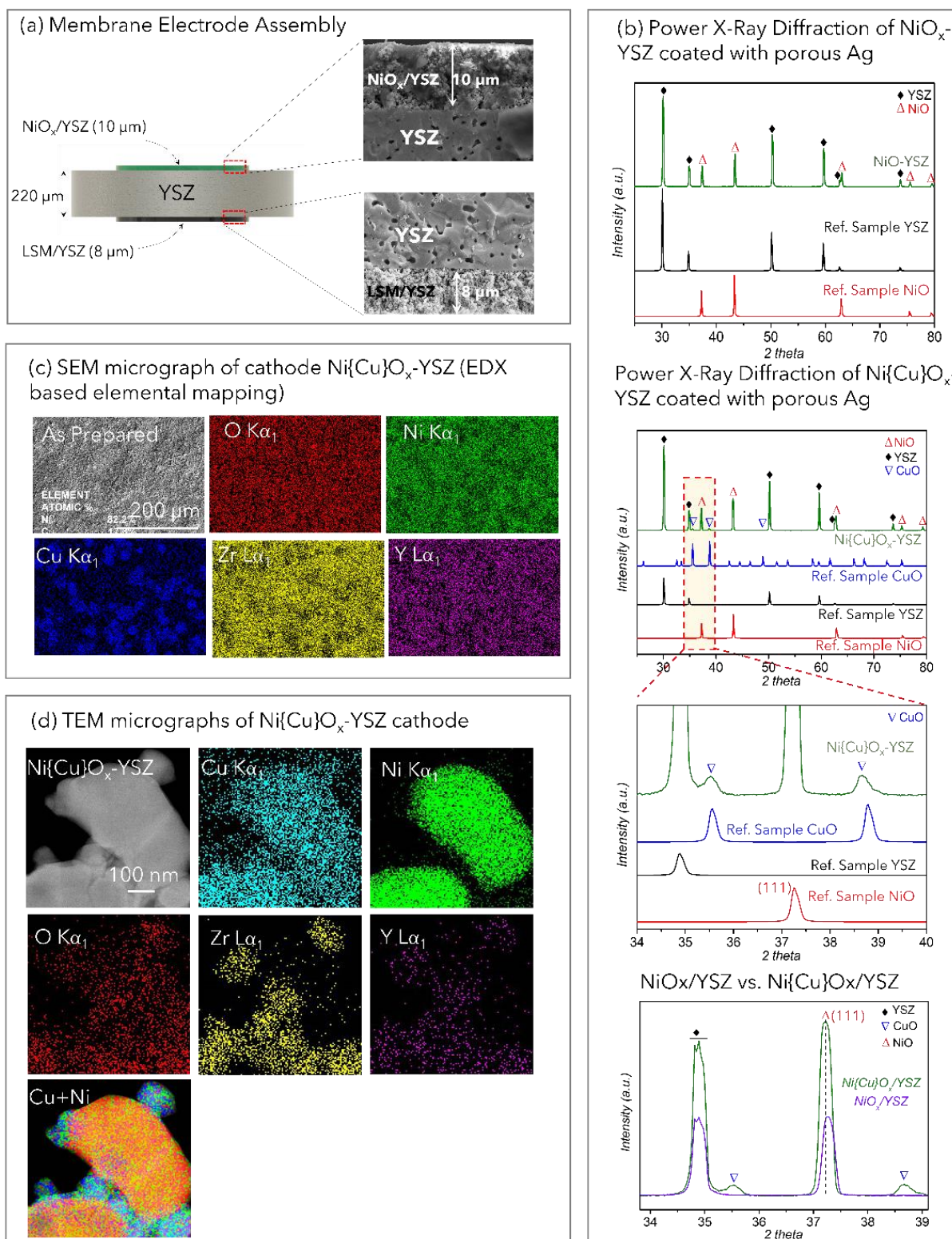


Figure 2: The cathode (NiO-YSZ, Ni{Cu}O_x-YSZ) was evaluated post-Cu impregnation and annealing step. The electrodes shown have not been reduced under hydrogen. (a) Membrane electrode assembly used for the studies. The interfaces of the cathode (NiO/YSZ) and anode (LSM/YSZ) with electrolyte (YSZ) are shown. (b) The PXRD patterns for NiO-YSZ and Ni{Cu}O_x-YSZ electrodes are shown. The

reference samples have been obtained from ICDD (international center for diffraction data). The JCPDS numbers have been reported in the supporting section (**Supplementary note 2**). (c) SEM images of the cross-section of NiO_x-YSZ/YSZ/LSM-YSZ cell are shown. The average composition of Cu was found to be $\sim 20 \pm 3\%$ and that of Ni to be $\sim 80 \pm 3\%$ using EDX (d) The STEM images of Ni{Cu}O_x-YSZ were collected in HAADF mode. Elemental mapping was performed using EDX.

The Cu-impregnated samples were annealed at 800°C and characterized using PXRD and electron microscopy (**Figure 2**). **Figure 2(a)** shows the membrane electrode assembly and cross-section SEM images showing the anodic and cathodic–electrolyte interfaces; of NiO-YSZ/YSZ and LSM-YSZ/YSZ. The cathode and anode were sufficiently porous and adhered well to the electrolyte. **Figure 2(b)** shows the PXRD patterns of NiO-YSZ and Ni{Cu}O_x-YSZ. The NiO-YSZ sample compares well with NiO and YSZ reference spectra indicating that the pure NiO phase is present alongside YSZ. The Ni{Cu}O_x-YSZ sample shows that this material is a combination of NiO, CuO, and YSZ phases. Comparison of the peaks shifts for these materials shows that NiO(111) diffraction peak is shifted upon adding Cu indicating the mixing of Cu into the NiO lattice (**Figure 2(b)**, bottom panel). SEM-EDX mapping (**Figure 2(c)**) indicates heterogeneity in Cu (Cu K α_1) distribution on the Ni-YSZ surface upon impregnation of Cu. TEM-EDX-based mapping indicates that NiO particles are linked via YSZ linkages (co-localization of Zr and Y distribution is seen). Cu impregnation and annealing treatment results in complete coverage of NiO-YSZ surface by CuO.

Operando Raman Spectroscopy

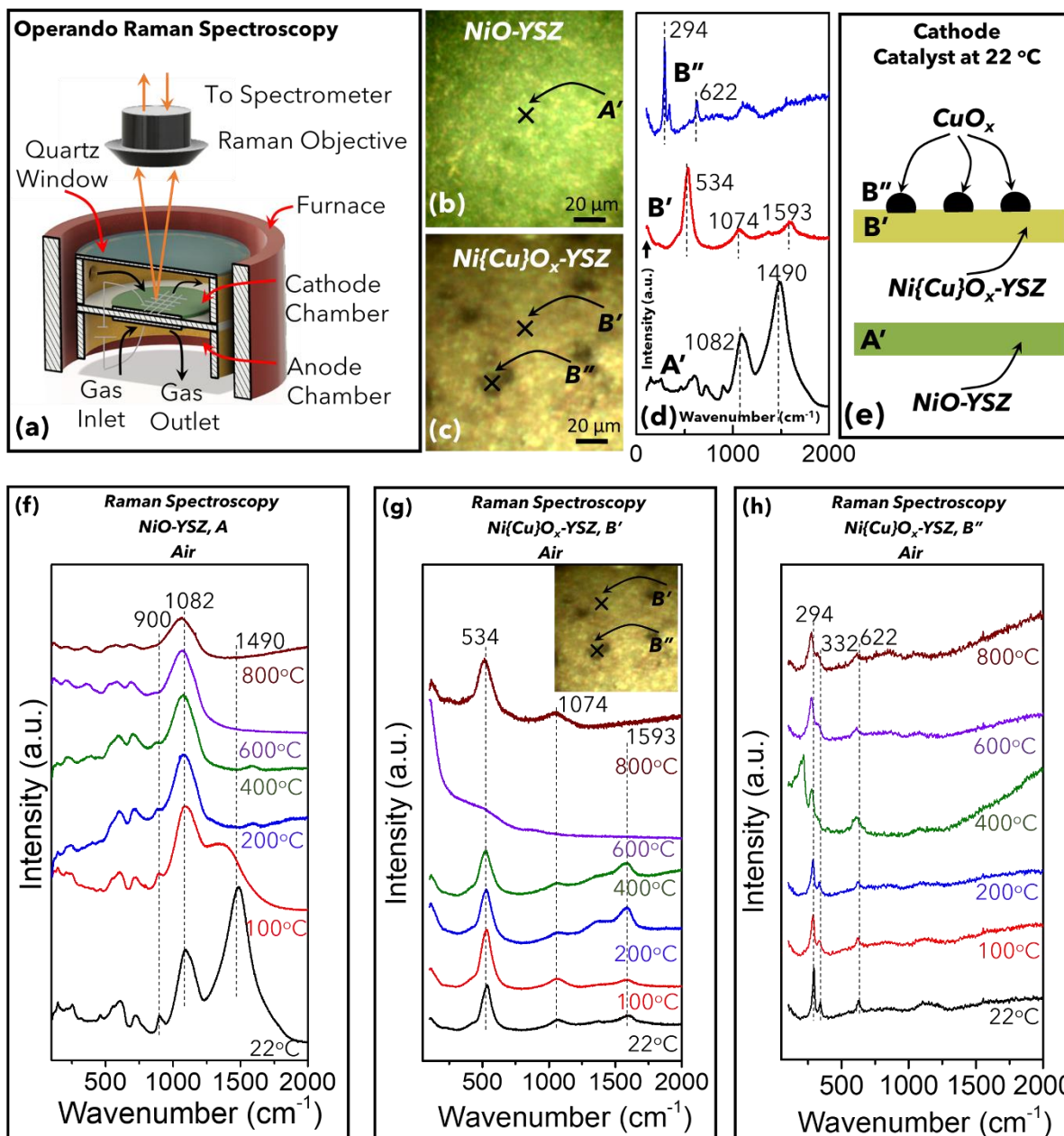


Figure 3: (a) Schematic diagram of operando Raman cell used in these studies. Optical images of (b) NiO-YSZ (c) Ni{Cu}O_x-YSZ (d) Raman spectra at the corresponding spots, (e) Schematic diagram of cathode architecture. Raman spectra of (f) NiO-YSZ, (g) Ni{Cu}O_x-YSZ, at B' site, and (h) Ni{Cu}O_x-YSZ, at B'' site recorded at different temperatures during heating from 22°C to 800°C in artificial air (20% O₂+80% Ar).

A two-chamber setup designed in-house was used for operando Raman studies (**Figure 3(a)**). The porous Ag current collector layer was partially removed from the top of the catalyst layer so that the NiO-YSZ particles could be directly visible under the Raman microscope. Sufficient conductivity was observed in active samples (containing Ni or Ni{Cu}O_x-YSZ) to maintain and monitor the triple-phase boundary regions that were electro-catalytically responsive. Studies by Kim. et al. have reported single chamber (cathode and anode on the same side) in situ Raman spectroscopic studies in the context of oxygen reduction reaction (ORR).⁴⁶ We are reporting results from a two-chamber cell (cathode and anode in different atmospheres) that simulates the conditions likely to be found within a real electrolyzer. Optical images corresponding to NiO-YSZ and Ni{Cu}O_x-YSZ cathodes are shown in **Figure 3(b, c)**. For NiO-YSZ, the surface was green in color, while Ni{Cu}O_x-YSZ surface was golden along with the presence of dark spots. The reported Raman spectra in **Figure 3(b,c)** were recorded at 22°C in artificial air (20% O₂ + 80% Ar). The spots for the Raman spectral collection have been marked with “x” and labeled with **A'**, **B'** and **B''** as shown in **Figure 3(d)**. The spectrum of spot A' corresponds to the NiO-YSZ electrode with peaks at 146 cm⁻¹, 225 cm⁻¹, 319 cm⁻¹, 460 cm⁻¹, and 604 cm⁻¹ corresponding to B_{1g}, E_g, B_{1g}, E_g, A_{1g}, and E_g vibration modes of YSZ respectively.⁴⁷ A more detailed spectrum is provided in **Supplementary Note 3**. The peak appearing at 562 cm⁻¹ corresponds to 1P (1 phonon) oscillations in NiO. The peaks at ~725, 900, and 1082 cm⁻¹ are attributed to the 2P oscillations in nickel oxide. Apart from this, the peak at ~1490 cm⁻¹ arises due to magnon (2M) oscillations.⁴⁸ Raman spectra of B' spot shows peaks at 225, 534, 1074, 1372, and 1593 cm⁻¹. The peak at 534 cm⁻¹ confirms the presence of Cu-doped Ni oxide (Cu alloyed into Ni oxide).⁴⁹⁻⁵¹ Spectrum at B'' on Ni{Cu}O_x-YSZ surface shows peaks at 294, 342, and 622 cm⁻¹ corresponding to A_g, B_g, and B_g vibrational modes of CuO.⁵² More details are available in **Supplementary Note 3**.

Figure 3(e) shows the schematic diagrams of electrode surfaces of both pure Ni-YSZ and its Cu-infiltrated counterpart. Whereas the pure material is composed of NiO as expected, the Cu infiltrated material is heterogenous at room temperatures with pure CuO patches (**B''**) present on a Cu-doped nickel oxide surface (**B'**) as confirmed using SEM-EDX mapping in the previous section.

In situ Raman spectra collected during cell heating (22°C temperature to 800°C) are reported in **Figure 3(f-h)**. For NiO-YSZ, upon heating, the 2M peak of NiO shifts to a lower wavenumber and eventually disappears at 200°C, as per the well-known magnetic behavior of this material.⁵³ No significant change in material phase was observed other than the expected redshift shift of peaks with increasing temperature (due to volume expansion).⁵⁴ The peak at 1082 cm⁻¹ redshifted by 31 cm⁻¹ upon heating to 800°C. For Ni{Cu}O_x, peaks around 1350-1595 cm⁻¹ corresponding to pore-forming carbon are completely removed by 800°C as the sample is heated in air (**Figure 3(g)**). The CuO patches (**Figure 3(e)**) remain upon heating to 800°C.

The cathode was subsequently reduced by using 5% H₂ in Ar. Concurrently, an artificial air atmosphere (20% O₂ in Ar) was maintained at the anode. The process was terminated when a stable open-circuit voltage (OCV) between the two electrodes was arrived at (1.1V after ~15 minutes, **Figure S2(a)**). The decay in the detected H₂O signal confirmed the completion of the process (**Figure S2(b)**).

a. Electrochemical characterization

A customized 2-chamber setup was used for electrochemical testing coupled with an online mass spectrometer as shown in **Figure S17(a)**. **Figure 4(a)** shows the current-voltage performance of CO₂ electrolysis at 800°C for both Ni-YSZ and Ni{Cu}-YSZ electrodes. The measurements were carried out in a 3-electrode geometry. The cathode voltage is reported vs. Ag/Pt electrode. A reduction current was progressively applied (current density J varied between 0 A/cm² and -0.48 A/cm²) in steps of 40 mA/cm². The current was held for 60 seconds at each step (**Figure S17(b)** shows currents maintained for 240 s at each potential step, no differences in behavior were observed). Mass signals were monitored simultaneously for reactions at both the cathode and anode. Electrochemical Impedance Spectroscopy (EIS) measurements were carried out at various applied currents (including at OCV). The uncompensated resistance (R_s) was extracted from the high-frequency intercept. All potentials have been corrected with obtained R_s value ($E_{\text{cathode}} = E_{\text{applied}} - iR_s$) in **Figure 4(b)**. The progressive application of cathodic current resulted in increased production of CO and consumption of CO₂ (**Figure 4(c)**). This continued up to 240 mA/cm² (@ -1.9V vs. Ag/Pt). At currents higher than this value, the

production of CO decreased, and the CO₂ consumption decreased as well, indicating deactivation. Subsequently, the cathode was switched between 480 mA/cm² and open circuit (each condition maintained for 3 minutes, while mass signals were continuously monitored). Application of 480 mA/cm² resulted in an instant increase in CO production followed by immediate deactivation.

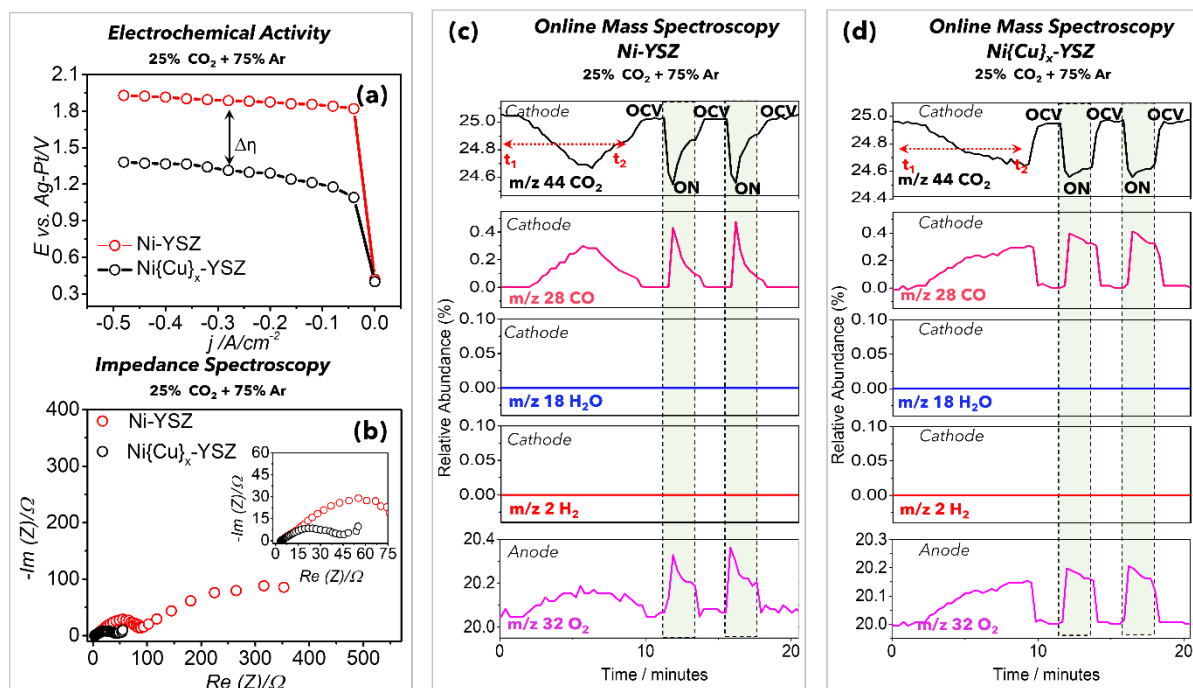


Figure 4: Performance of Ni-YSZ and Ni{Cu}_x-YSZ cathodes. (a) Applied current vs. potential curves for electrochemical reduction of CO₂, (b) EIS plots under open-circuit conditions, Cathodic and anodic MS signal (c) Ni-YSZ (d) Ni{Cu}_x-YSZ, in the presence of 25% CO₂ at 800 °C.

Cu infiltration into the Ni-YSZ electrode (**Figure 4(a)**) resulted in a significant decrease in potential ($\Delta\eta = 0.58$ V) required to achieve -240 mA/cm² during pure CO₂ electrolysis. A significant reduction in the polarization resistance was observed in the impedance spectra indicating superior electrocatalytic performance(**Figure 4(b)**). The cathodic and anodic online mass signals from reactions from Ni-YSZ and Ni{Cu}_x-YSZ electrodes during CO₂ electrolysis are shown in **Figure 4(c, d)**. In the case of Ni{Cu}_x-YSZ cathode there is a progressive increase in the amount of CO formation with an increase in applied current density. Unlike Ni-YSZ, the CO signal does not decay after 240 mA/cm² but rather continues to increase all the way up to 480 mA/cm². Once at 480 mA/cm², the CO mass signal is

reasonably maintained at a constant current. Contrastingly, in the case of the Ni-YSZ cathode (as discussed earlier), the onset of CO production (jump in CO production mass signal) upon stepping up to 480 mA/cm² is immediately followed by a catastrophic decay in the CO formation signal.

b. Verification of electrode oxidation and Boudouard reaction

Previously, it has been proposed that Ni catalyst deactivation during pure CO₂ electrolytic reduction results from reactions such as Ni oxidation and Boudouard reaction (**Figure 5(a)**).^{35,37} The experimental scheme shown in **Figure 5(b)** was used to probe the formation of C_x and metal oxide(s) species on the electrode surface from reactions (1) and (2) respectively. Mass signals were monitored during the entire scheme of experiments. In the reaction regime **A**, electrolysis was carried out at 480 mA/cm² for the time duration of t₁ – t₂. The current was switched off and the electrode was allowed to stay in the CO₂ atmosphere (25% CO₂ in Ar) during t₂ – t₃. Then CO₂ was switched off and the electrode was exposed to 100% Ar during t₃ – t₄ (regime **B**). Subsequently, the electrodes were exposed to either 1% O₂ (in Ar) (**C'**) or 5% H₂ (in Ar) (**C**).

Figure 5(c-f) shows the above experimental scheme applied to Ni-YSZ and Ni{Cu}_x-YSZ electrodes. On Ni-YSZ, the introduction of 5% H₂ resulted in the formation of H₂O on both electrodes indicating that electrodes get oxidized during reaction regime **A**. The H₂O mass signal obtained from identical experiments on two different electrodes indicated that the amount of oxide formed on Ni{Cu}_x-YSZ is less compared to the Ni-YSZ electrode. The H₂O signal from the Cu-doped counterpart is not only smaller, but the reduction process also gets completed in half the time (~20 mins) as opposed to on the Ni-YSZ electrode. Similarly, exposure to 1% O₂ resulted in developing a mass signal for CO₂ (m/z = 44) indicating that reaction regime **A** does result in the formation of C_x species on the surface of the electrode via the Boudouard reaction. No carbon deposit formation could be inferred on Ni{Cu}_x-YSZ using mass spectroscopy.

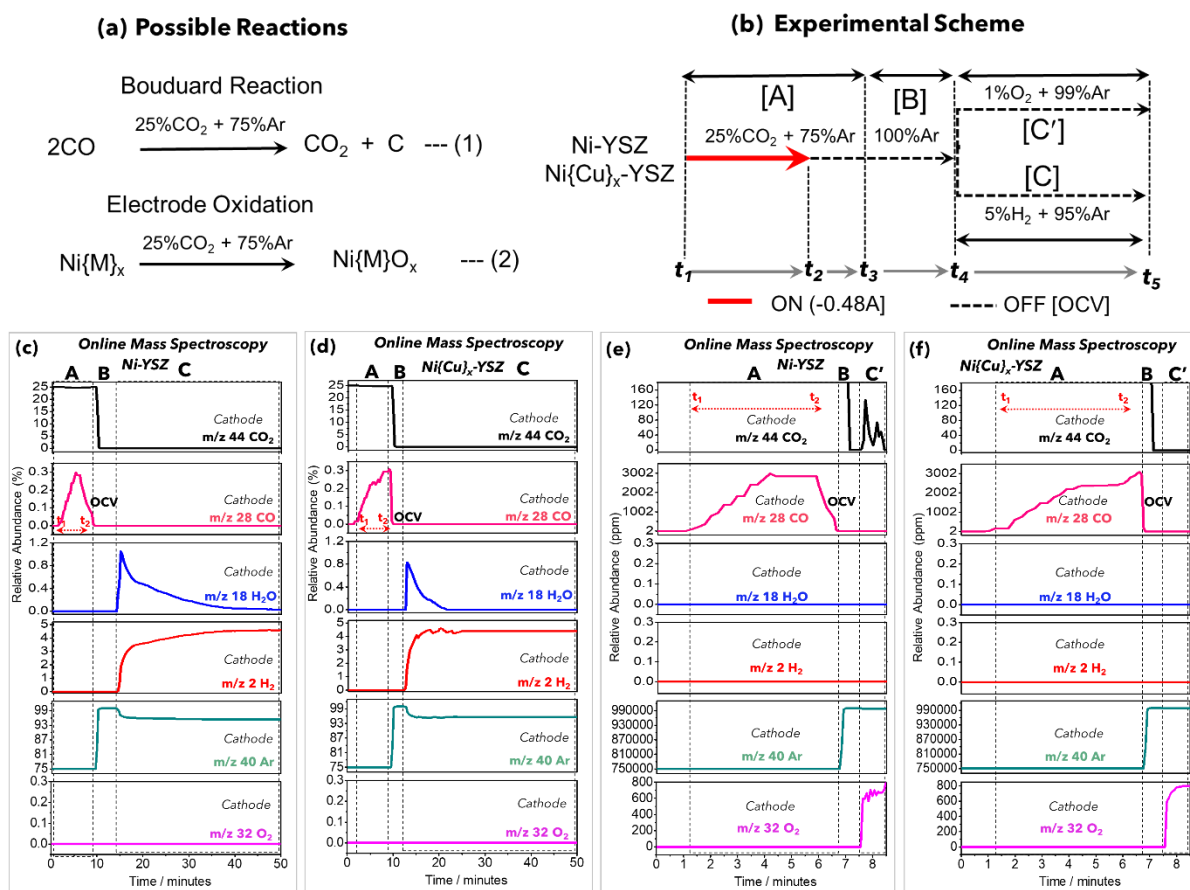


Figure 5: (a) Possible side reactions during CO₂ electrolysis (b) Experimental Scheme to probe reactions mentioned in (a). After treating the catalyst at -0.48 mA/cm² under 25% CO₂, the catalyst is treated at OCV under 100% Ar atmosphere. Subsequent treatment in 5% H₂ [C] and 1% O₂ [C'] was carried out to confirm the presence of oxides (NiO_x/Ni{Cu}O_x) and carbon on the electrode surface. The mass signals from Ni-YSZ (c,e) and Ni{Cu}_x-YSZ (d,f) electrodes are shown.

Impedance Spectroscopy:

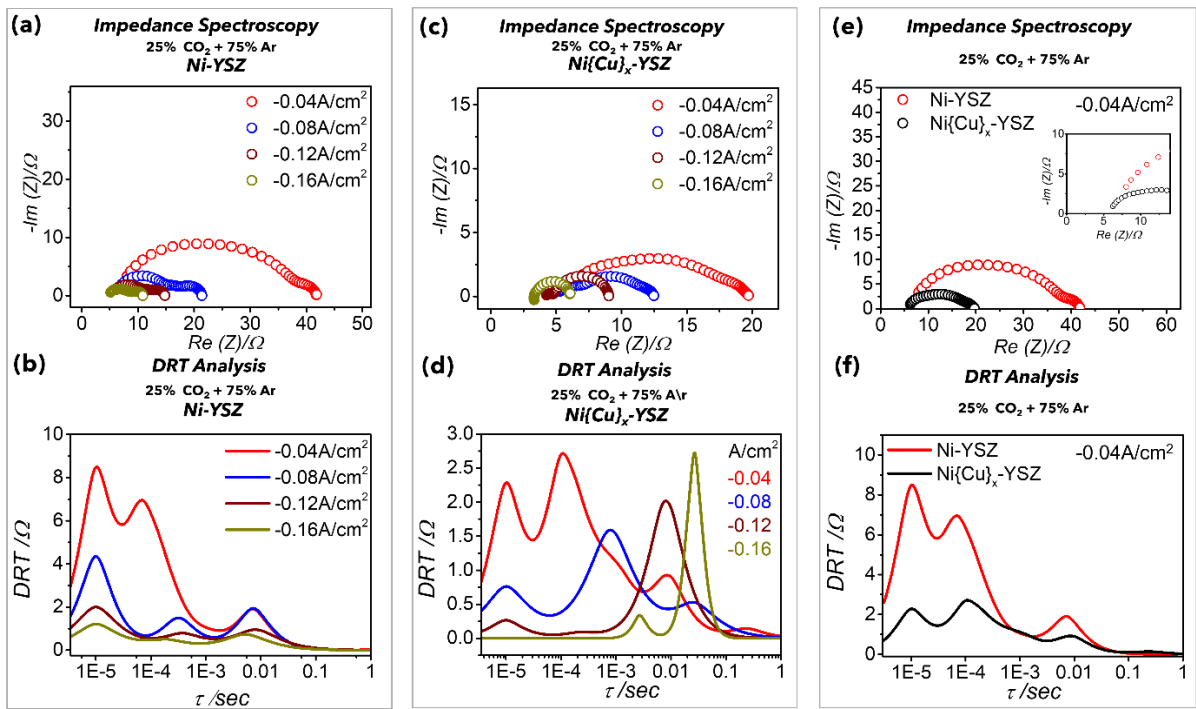


Figure 6: EIS under CO_2 electrolysis conditions for various applied current densities (a) Ni-YSZ (b) DRT plot for Ni-YSZ. (c) $\text{Ni}\{\text{Cu}\}_x\text{-YSZ}$ (d) DRT plot for $\text{Ni}\{\text{Cu}\}_x\text{-YSZ}$ (e) Comparison of Ni-YSZ and $\text{Ni}\{\text{Cu}\}_x\text{-YSZ}$ electrodes at -0.04 mA/cm^2 . (f) DRT plots for of Ni-YSZ and $\text{Ni}\{\text{Cu}\}_x\text{-YSZ}$ electrodes.

To understand the improvement in the performance of $\text{Ni}\{\text{Cu}\}_x\text{-YSZ}$ cathode, impedance spectra of Ni-YSZ and $\text{Ni}\{\text{Cu}\}_x\text{-YSZ}$ cathode were recorded at different applied current densities during CO_2 electrolysis. With an increase in current density, cell resistance decreased slightly, while a drastic reduction in polarization resistance is observed (**Figure 6(a)**). Distribution of Relaxation Times (DRT) analysis was carried out on EIS data to separate out contributions to the electron transfer processes at different timescales **Figure 6(b)**. DRT plot showed three distinct peaks. The high-frequency peak could be attributed to charge transfer resistance, the intermediate-frequency peak could be attributed to surface exchange, and the low-frequency peak could be attributed to diffusion, based on similar data analysis by Chen et al. and Kim and coworkers for oxygen reduction reaction in perovskite materials.^{55,56} A reduction in charge transfer resistance at higher current densities can be inferred from the high-frequency component of the Ni-YSZ DRT spectra (**Figure 6(b)**). The contributions from the middle decrease, but those from low-frequency components remain. The overall impedance was smaller for $\text{Ni}\{\text{Cu}\}_x\text{-YSZ}$ electrode. The contribution of the high-frequency component was significantly reduced

at higher current densities indicating faster kinetics. At high current densities, the reaction on Ni{Cu}O_x-YSZ became essentially diffusion-limited with a large contribution from low-frequency component (**Figure 6(c, d)**). At low current densities (-40 mA/cm²), where Ni-YSZ was found to be active for CO₂ reduction, the improved performance of Ni{Cu}_x-YSZ cathode can be attributed primarily to better surface exchange, charge transfer (difference in the high and intermediate-frequency components (**Figure 6(e, f)**)).

c. Operando Raman spectroscopy

Operando Raman spectroscopy of Ni-YSZ electrode was carried out post reductive treatment in 5% H₂ (at 800°C) shown in **Figure S18(e, I)**. The peaks including 599 cm⁻¹ can be assigned to YSZ, indicating that all Ni is present in a reduced metallic state (**Figure S18(e) I**). The reduced electrode was then exposed to 25% CO₂ (in Ar) at 800°C and developed peaks at 343, 509, 684, and 1051 cm⁻¹ (**Figure S18(e) II**). These peaks can be attributed to the oxide of Ni, indicating that exposure to 25% CO₂ at 800°C (at OCV) is sufficient to develop an oxide on Ni. The peaks at 343, 684, and 1051 cm⁻¹ appear in NiO (**Figure 3(f)**). A strong peak at 509 cm⁻¹ was also observed. The PXRD pattern of this oxide (**Figure S9**) matches with NiO, similarly Ni_{2p} levels observed in XPS (**Figure S12**) indicate similarity to NiO indicating that this is possibly a defective form of NiO, hereby referred to as NiO_x. Subsequently, a reducing current was applied (-480 mA/cm²) while the electrode was maintained in this atmosphere (25% CO₂) simulating a condition where electrolysis happens under a strong reducing condition. Raman spectrum of this electrode (**Figure S18(e) III**) only showed peaks corresponding to YSZ, while the NiO signal completely vanished indicating that NiO converts back to Ni under strongly reducing conditions (deactivated electrode).

Operando Raman spectra were recorded at various applied cathodic current densities during CO₂ electrolysis (**Figure S19(a)**). The electrode showed a strong NiO_x signal at the open circuit. Upon applying increasing cathodic currents progressively, the NiO_x signal intensity decreased and eventually vanished after 300 mA/cm² (**Figure S19(a)**). The detection of CO in the mass spectrometer exactly followed the same trend with respect to the applied currents. A direct correlation of the detected CO

mass signal to the intensity of NiO_x peaks on the electrode surface was observed. The CO production peaked at 240 mA/cm² and then degraded. The NiO_x signal on the electrode surface was observed from OCV up to 200 mA/cm² and then begins to degrade coinciding with the decay of the CO mass signal. This indicates that CO₂ is reduced at an electrode that is composed of NiO_x rather than Ni. The NiO_x is formed at the open circuit, and with increasing overpotential, the reduction of NiO_x competes with CO₂ reduction on the electrode. As the current density increases, the amount of NiO_x progressively decreases (Raman intensities, **Figure S19(a)**) and eventually disappears. Since the current density for complete reduction of catalyst (NiO_x disappearance) matches the current density at which decay in the CO production (and CO₂ consumption) occurs, it indicates that there is a significant decrease in the number of active sites for CO₂ electrolysis due to conversion of NiO_x to Ni.

Upon switching the electrode between 480 mA/cm² (strongly reducing condition) and OCV, the catalytic behaviour of CO₂ reduction along with deactivation of the electrode can be recreated. The Raman spectra on the Ni electrode shows that under conditions of electrolysis NiO_x gets regenerated when OCV is created and is completely removed once a strongly reducing current of 480 mA/cm² is applied. Application of 480 mA/cm² resulted in a spike in the CO signal immediately followed by a decay in the signal indicating that the electrode gets deactivated (**Figure 4(c)**). Alternating the applied current between strongly reducing (480 mA/cm²) and OCV, showed that oxide creation was reversible (**Figure S19(b)**). The Raman spectra confirms it.

Figure S27 shows Raman spectra of both the cathodes at OCV, collected in artificial air (20% O₂ + 80% Ar), followed by a reduction in (5% H₂ + 95% Ar), and subsequently in the presence of 25% CO₂ + 75% Ar. For the Ni-YSZ electrode (**Figure S27(a)**), the NiO was observed in both artificial air and CO₂ (peaks in air and CO₂ are similar with the earlier noted difference in 509 cm⁻¹ peak), whereas in the presence of 5% H₂, the oxide was completely reduced, and only peaks attributed to YSZ could be observed. In artificial air, Raman spectrum at B' showed peaks at 520 and 1057 cm⁻¹ corresponding to the formation of Cu doped-Ni oxide (**Figure S27(b)**) while B'' spot showed peaks at 273 and 316 cm⁻¹ corresponding to CuO as shown in **Figure S27(c)**. A reduction in 5% H₂ resulted in the complete

removal of oxide peaks at both B' and B''. Exposure to CO₂ again resulted in the appearance of the same oxide peaks indicating oxidation in CO₂ in both Ni-YSZ and Ni{Cu}_x-YSZ electrodes.

During CO₂ electrolysis at 480 mA/cm², the Ni in Ni-YSZ, present as NiO_x at OCV, is completely reduced back to metallic Ni (**Figure S28(a)**). For Ni{Cu}_x-YSZ, the application of 480 mA/cm² results in changes at two different sites identified in **Figure 3(c)**. At B', the site which is composed of Cu-doped Ni oxide, the intensity of oxide peaks decreases but does not disappear ((**Figure S28(b)**). At B'', the site which was rich in CuO, the peak at 273 cm⁻¹ (corresponding to CuO peak) vanished completely, and the peak at 520 cm⁻¹ (corresponding to Cu doped Ni oxide) reduced in intensity. It was observed that sites like B'' although initially rich in CuO change in composition to B' type sites upon electrode cycling (reoxidation and reduction)(**Figure S31**). Such sites (B'') can be understood as those where Cu atoms have not completely mixed with Ni to form a mixed oxide during impregnation and consequent heat treatment. But eventually, as the electrode is repeatedly exposed to high temperatures (800°C) and repeated oxidation and reduction processes such Cu-rich sites eventually disappear due to diffusion of Cu into the electrode creating a mixed Ni-Cu material which when reoxidized (in CO₂) results in the formation of Cu-Ni mixed oxide. EDX data also confirms that Cu redistributes into the electrode uniformly (**Figure S6-S7**). Hereon, we would primarily focus the discussion on B' (Cu-doped Ni).

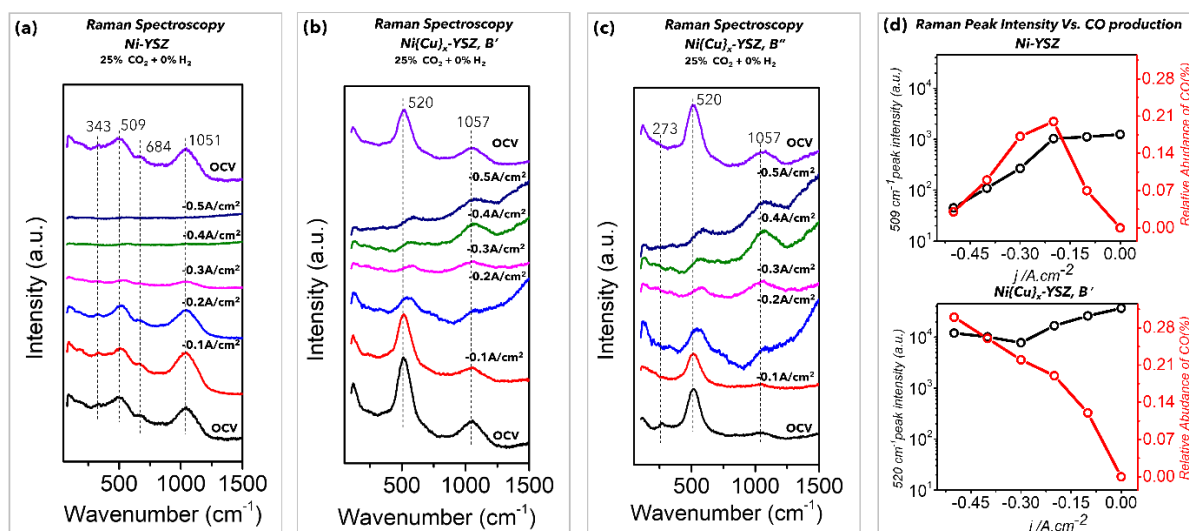


Figure 7: Operando Raman Spectra during CO₂ electrolysis at various current densities. (a) Ni-YSZ electrode (b) Ni{Cu}_x-YSZ, B' site (c) Ni{Cu}_x-YSZ, B'' site, d) Raman peak intensity plotted against the abundance of CO in the product stream of various electrodes. Raman spectra at Ni-YSZ and Ni{Cu}_x-YSZ, B' site are shown.

Operando Raman spectra collected at progressively increasing applied cathodic currents during CO₂ electrolysis are shown in **Figure 7**. The peaks observed on the Ni-YSZ electrode (corresponding to NiO_x)(**Figure 7(a)**) decrease in intensity as the currents increase. The peaks are of negligible intensity by 300 mA/cm² and completely disappear by 400 mA/cm². For the Ni{Cu}_x-YSZ electrode (**Figure 7(b)**), the peaks corresponding to Cu-doped Ni oxide decrease in intensity with a progressive application of reduction current (in CO₂), but never disappear. At site B'', the peak at 273 cm⁻¹ (assigned to CuO) vanishes on applying 100 mA/cm² but the remaining set of peaks corresponding to Cu-doped Ni oxide show a behavior similar to that at B' (**Figure 7(c)**).

Peak intensities of representative peaks (for both electrodes) and the abundance of CO in the product stream have been plotted against the applied current density (**Figure 7(d)**). In the case of the Ni-YSZ electrode, the drastic decrease in peaks' intensity beyond 200 mA/cm² coincides with the decrease in CO production. This indicates that a certain minimum amount of oxide is necessary for continued CO₂ electro-reduction, as complete removal of oxide coincides with catalytic deactivation. For the Ni{Cu}_x-YSZ electrode, although the amount of oxide reduces upon increasing the reduction current, the amount of oxide on the electrode stabilizes around 200 mA/cm² and remains constant even at higher currents, the electrode does not deactivate.

An alternating application of 480 mA/cm² and OCV on both Ni-YSZ and Ni{Cu}_x-YSZ electrodes is shown in **Figure S29**. Whereas a complete removal of metal oxide is seen in Ni-YSZ upon application of 480 mA/cm², the oxide remains on Ni{Cu}_x-YSZ electrode.

The H₂O mass signal in **Figure 5(a,b)**, in combination with operando Raman spectroscopy indicates that the oxide layer formed on Ni{Cu}_x-YSZ is thinner but more stable to electrochemical reduction under a CO₂ electrolysis environment. No carbon deposit formation could be inferred through either

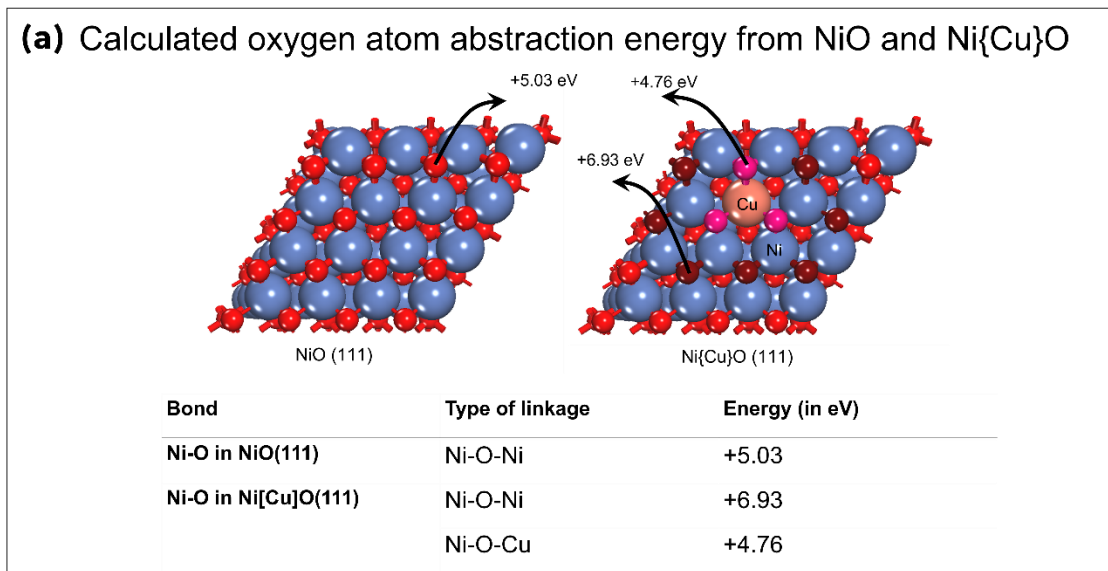
mass spectroscopy or Raman spectroscopy on the Ni{Cu}_x-YSZ cathode, indicating an absence of Boudouard reaction on this electrode.

Figure S33(a,b) shows the current-voltage performance of Ni-YSZ and Ni{Cu}_x-YSZ cathodes in two cycles of CO₂ electrolysis. Each cycle takes the electrodes from OCV up to 480 mA/cm² at 40 mA steps and then creates an open circuit. A single cycle results in a substantial increase of overpotential at Ni-YSZ, indicating a significant loss of active sites during the previous cycle. A third such cycle could not be carried out on Ni-YSZ as the electrode completely degraded. It is likely that repeated oxidation (NiO_x formation) and complete electrochemical reduction back to Ni may lead to the degradation of ionic connections resulting in electrode breakdown. More information on the degradation of Ni-YSZ is available in **Figure S34**. On the other hand, the Ni{Cu}_x-YSZ electrode does not degrade with the same sequence of current cycling. The current potential curve during the second cycle exactly retraced the first, indicating no degradation.

Reducibility of metal oxides

In the light of results obtained from operando studies, further studies on the stability of NiO, CuO, and Ni{Cu}O_x were carried out both using theoretical calculations (**Figure 8(a)**) and temperature programmed reduction (TPR) experiments (**Figure 8(b)**). Theoretical calculations (Density Functional Theory) which estimate oxygen abstraction energies from these oxides were carried out ($E_{\text{abs}} = (E_{\text{O}} + E_{\text{MO}'} - E_{\text{MO}})$) where E_{abs} is the energy of O abstraction (electronic energy), E_{MO} is the energy of the metal oxide and $E_{\text{MO}'}$ is the energy of the defective metal oxide (where one oxygen atom has been removed), and E_{O} is the energy of a free oxygen atom. A higher abstraction energy implies a greater degree of difficulty in oxygen atom removal or higher oxophilicity of the particular oxide. It was observed that doping with Cu atoms resulted in the enhancement of E_{abs} of oxygen atoms within Ni-O-Ni bonds (by nearly 1.9 eV). The oxygen bound to Ni-O-Cu bonds became slightly easier to abstract with E_{abs} of 4.76 eV compared to Ni-O-Ni bonds in pure NiO (at 5.03 eV). Calculations indicate that doping NiO with Cu results in a bimodal distribution of oxygen abstraction energies, whereas some

oxygen atoms become slightly easier to abstract, other oxygen atoms, those within Ni-O-Ni become much more difficult to abstract.



(b) Temperature Programmed Reactivity of NiO, CuO and Ni{Cu}O_x in H₂

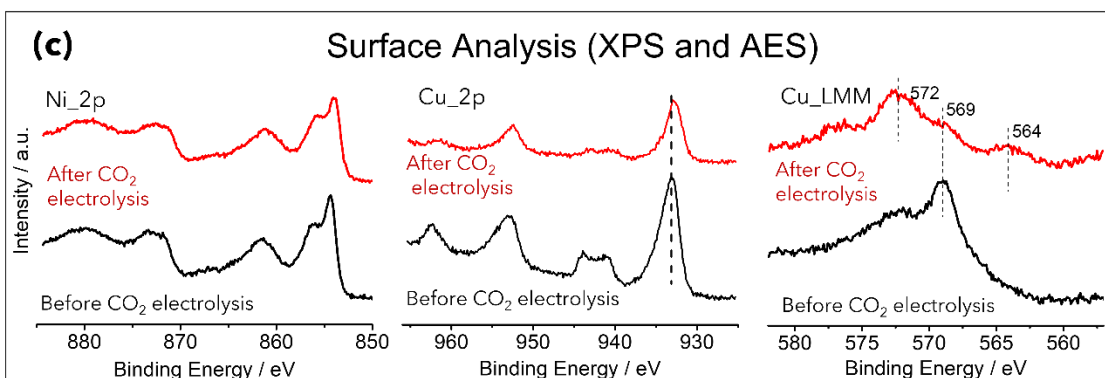
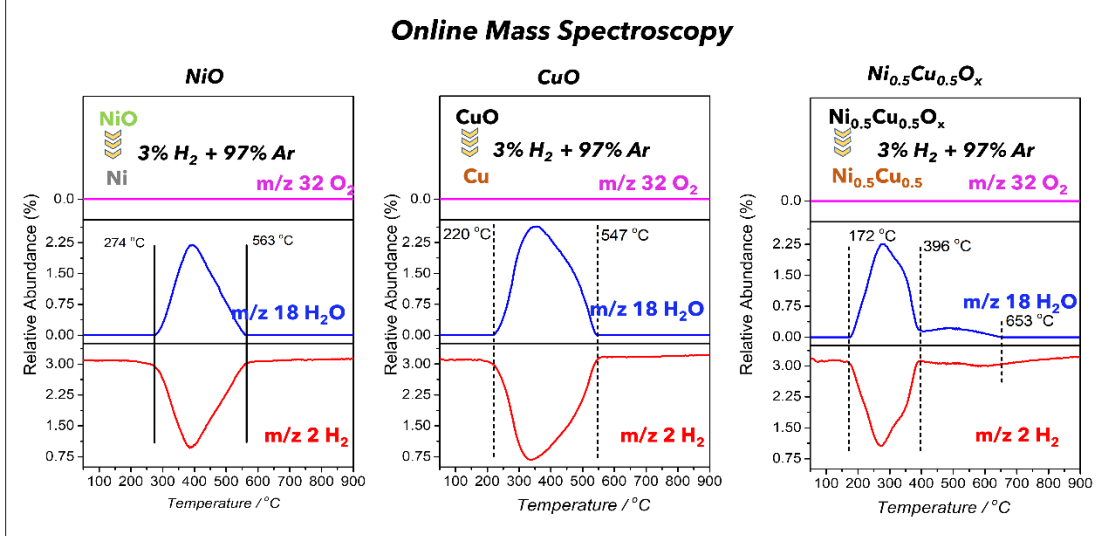
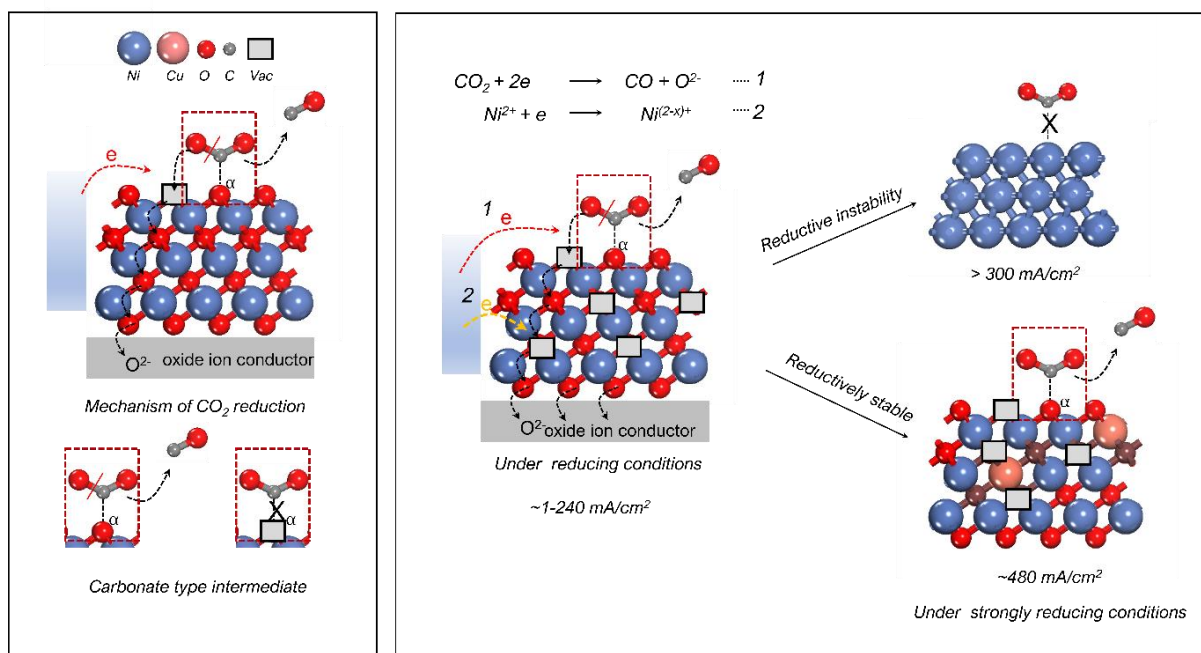


Figure 8: (a) Oxygen atom abstraction energies calculated from NiO and Ni{Cu}O structures. (b) Temperature programmed reduction in 3% H₂ (in Ar) for pure NiO, CuO, and Ni_{0.5}Cu_{0.5}O. The mass signals for H₂O (m/z 18), H₂ (m/z 2), and O₂ (m/z 32) were continuously monitored. (c) Ni 2p and Cu 2p, and CuLMM signals for samples were collected before and after CO₂ electrolysis. The pre-electrolysis signals (black) are those from Ni{Cu}O oxide (post impregnation and annealing at 800°C) before sample reduction, and post-electrolysis samples (red) were obtained by cooling the samples under 25% CO₂ (in Ar) at OCV.

The TPR experiments were performed on NiO, CuO, and Ni{Cu}O powders. These powders were synthesized using solution-based precursors (co-precipitation method) guaranteeing atomic-level mixing of metals within the metal oxide framework. More information on the synthesis and characterization of these powders is provided in the supporting information (**Supplementary Note 3, VII**). TPR experiments using 3% H₂ (in Ar) were performed on various compositions of Ni_{1-0.5}Cu_{0-0.5}O_x (**Figure 8 (b)** and **Figure S25-26**). Measurements indicate that H₂O removal peaks in pure NiO and pure CuO range between 274-563°C and 220-547°C respectively. Mixing NiO with Cu results in a bimodal distribution of oxygen removal (H₂O signals) signal. The sample with 50% Cu doping showed oxygen removal between 172-396°C and between 396 and 653°C. Such a distribution is also visible in other samples where Cu doping is between 10 and 40%. These experiments are consistent with theoretical calculations where doping with Cu within NiO seems to both reduce and increase O abstraction energies within the oxide. The high-temperature stability introduced by mixing Cu also gets reflected within the higher stability to reduction of Ni{Cu}O_x electrodes. XPS and AES were used to probe the surface of the catalysts before and after CO₂ electrolysis (**Figure 8(c)** and **Figure S12-14**). In the latter case, the catalysts post CO₂ reduction, at OCV was created, and the electrode was cooled from 800°C to room temperature in a CO₂ atmosphere (same as reaction atmosphere). Ni 2p spectra indicate that Ni retains essentially the same features before and after CO₂ electrolysis, an oxidation state of Ni²⁺. This is also similar to pure NiO/YSZ electrodes. The Cu 2p spectra in the pre-electrolysis sample have features similar to CuO indicating Cu is in a +2 oxidation state. Post CO₂ reduction, the satellite features (945-940 eV) reduce in relative intensity, and the peak at 933.1 shifts to lower binding energies

indicating the reduction of Cu. Distinguishing between Cu^{1+} and Cu^0 remains challenging using Cu 2p spectra as binding energy differences are minute between the two. AES (Cu LMM) peaks better distinguish between Cu oxidation states. Peaks at 564 and 569 eV indicate that the sample has both Cu^0 and Cu^{2+} in the sample. This indicates that in $\text{Ni}\{\text{Cu}\}\text{O}_x$ electrode, Cu is in a reduced state post-electrolysis compared to the as-prepared $\text{Ni}\{\text{Cu}\}\text{O}_x$ before electrolysis.



Scheme 1: Proposed mechanism for CO_2 reduction on Ni electrodes is shown (left). The nature of electron transfer reactions (1, 2) is shown. Pure Ni shows reductive instability and reduces to Ni metal (at currents $>300 \text{ mA/cm}^2$) which is inactive for CO_2 reduction. The mixed Ni-Cu oxide has more strongly bound oxygen species on Ni which are reductively stable even at currents $\sim 480 \text{ mA/cm}^2$.

Mechanism of CO_2 reduction

In oxide cathodes such as $(\text{La}, \text{Sr})(\text{Co}, \text{Fe})\text{O}_x$ and SmCeO_x , it has been shown that CO_2 reduction proceeds via a carbonate type (3 coordinate carbon) type intermediate. The presence of oxygen atoms on the surface of the catalysts plays a vital role in the formation of such a species.^{28,57–59} **Scheme 1** shows the mechanism of CO_2 reduction on the surface of oxide electrodes. The surface oxygen, labeled α interacts with gas phase CO_2 to form a carbonate-type species. The presence of a vacancy nearby

helps in cleaving the C-O bond with the oxygen atom inserting into the oxide surface and transferring to the ionic conductor. Optiz et al. have proposed a similar surface oxygen and surface vacancy mediated carbonate type species formation.⁵⁹ Ye et al. have also shown the formation of carbonate-type species on {La, Sr}TiO_{3-x} using in situ IR spectroscopy in combination with TPD.¹⁷ In oxides, the CO₂ reduction process essentially competes with the reduction of the metal. Feng et al. have shown that the surface of Sm_xCe_{1-x}O₂ became enriched in Ce³⁺ (~45%) upon application of cathodic overpotential under CO₂ reduction. The anodic polarization on the other hand results in Ce⁴⁺ enriched surface. Albrecht et al. have shown using C k-edge NEXAFS on defective ceria (CeO_{1.7}), CO₂ to be preferentially adsorbed in the vicinity of Ce³⁺.⁶⁰ It is imperative that both surface oxygen species (α) and oxygen vacancy on the surface play an important role in the creation of a carbonate-type intermediate. Under reducing conditions, both CO₂ and NiO are likely to be reduced as shown in processes 1 and 2 respectively. Whereas the former is the desired reaction, the latter very likely assists in the process via the creation of vacancies that can interact with CO₂. A live catalyst is likely to have both species in balance. NiO catalyst does not degrade at currents of ~200 mA/cm² and can successfully reduce CO₂ to CO (**Figure S34**). At higher current densities > 240 mA/cm² the metal oxide reduction process seems to dominate, leading to a reduction in α oxygen-type active sites and decrease in CO production. At currents approaching 400 mA/cm², a complete reduction of oxide occurs, which does not allow for CO₂ to interact with the now pure Ni surface. The Ni{Cu}O_x, on the other hand is much more difficult to reduce owing to difficult to abstraction of oxygens within Ni-O-Ni linkages of the mixed oxide material which allows this material to have stability even under strongly reducing conditions. Importance of surface oxygen for CO₂ reduction is also highlighted by studies from Zhou et al. who have shown (using operando XANES/XAFS) that even in the aqueous medium, at ambient temperatures, CO₂ reduction to products involves sites containing Ni-O bonds (with Ni ^{$\delta+$}).⁶¹

Conclusion:

Operando Raman and online mass spectrometry experiments indicate that Ni-YSZ can be used for reducing pure CO₂ streams to CO. When the electrode is placed under reaction conditions at OCV, CO₂ creates an oxide on the Ni surface. It is this oxide surface that acts as the catalyst for CO₂ reduction.

CO₂ reduction and oxide reduction are competing processes, and CO₂ reduction proceeds via a surface oxygen and vacancy-mediated carbonate type intermediate. Although Ni-YSZ remains active around 200 mA/cm², at currents > 240 mA/cm², the catalyst begins to lose active sites resulting in decreased CO production. Under strongly reducing conditions (currents ~400 mA/cm²), the NiO_x completely reduces which coincides with stoppage in CO production. The Cu-impregnated Ni-YSZ results in a Ni{Cu}_x alloy, which forms a more stable mixed oxide in situ on the Ni surface. Theoretical calculations using DFT and TPR experiments indicate that oxide stability significantly increases upon mixing Cu with Ni. The oxygen within Ni-O-Ni (in Cu-doped material) linkages is significantly more stable to reduction compared to pure NiO. Such an oxide survives under strongly reducing conditions and remains active for CO₂ reduction. The Ni{Cu}_x-YSZ electrode also demonstrated improved kinetics and greater stability against the carbon deposition via the Boudouard reaction. Impedance analysis suggests that better surface exchange and reduction in charge transfer resistances are responsible for the improved kinetic performance of Ni{Cu}_x-YSZ electrode.

Author Information:

Vipin Kamboj: Experimental work, instrument design and fabrication, data analysis, and writing.

Soham Raychowdury: Theoretical calculations

Chinmoy Ranjan: Conceptualisation of project, design of experiments, instrument design, data analysis, and writing.

Supporting Information: Supporting information contains details of experiments, characterization, theory, and spectroscopic and catalytic data.

References:

- (1) Florides, G. A.; Christodoulides, P. Global Warming and Carbon Dioxide through Sciences. *Environ. Int.* **2009**, *35* (2), 390–401. <https://doi.org/10.1016/j.envint.2008.07.007>.
- (2) Mattia, D.; Jones, M. D.; O'Byrne, J. P.; Griffiths, O. G.; Owen, R. E.; Sackville, E.; McManus, M.; Plucinski, P. Towards Carbon-Neutral CO₂ Conversion to Hydrocarbons. *ChemSusChem* **2015**, *8* (23), 4064–4072. <https://doi.org/10.1002/cssc.201500739>.
- (3) Yuan, Z.; Eden, M. R.; Gani, R. Toward the Development and Deployment of Large-Scale Carbon Dioxide Capture and Conversion Processes. *Ind. Eng. Chem. Res.* **2016**, *55* (12), 3383–3419. <https://doi.org/10.1021/acs.iecr.5b03277>.
- (4) Kar, S.; Goeppert, A.; Galvan, V.; Chowdhury, R.; Olah, J.; Prakash, G. K. S. A Carbon-Neutral CO₂ Capture, Conversion, and Utilization Cycle with Low-Temperature Regeneration of Sodium

- Hydroxide. *J. Am. Chem. Soc.* **2018**, *140* (49), 16873–16876.
<https://doi.org/10.1021/jacs.8b09325>.
- (5) Küngas, R. Review—Electrochemical CO₂ Reduction for CO Production: Comparison of Low- and High-Temperature Electrolysis Technologies. *J. Electrochem. Soc.* **2020**, *167* (4), 044508.
<https://doi.org/10.1149/1945-7111/ab7099>.
 - (6) Ebbesen, S. D.; Mogensen, M. Electrolysis of Carbon Dioxide in Solid Oxide Electrolysis Cells. *J. Power Sources* **2009**, *193* (1), 349–358. <https://doi.org/10.1016/j.jpowsour.2009.02.093>.
 - (7) Chen, L.; Chen, F.; Xia, C. Direct Synthesis of Methane from CO₂-H₂O Co-Electrolysis in Tubular Solid Oxide Electrolysis Cells. *Energy Environ. Sci.* **2014**, *7* (12), 4018–4022.
<https://doi.org/10.1039/c4ee02786h>.
 - (8) Xie, K.; Zhang, Y.; Meng, G.; Irvine, J. T. S. Direct Synthesis of Methane from CO₂/H₂O in an Oxygen-Ion Conducting Solid Oxide Electrolyser. *Energy Environ. Sci.* **2011**, *4* (6), 2218–2222.
<https://doi.org/10.1039/c1ee01035b>.
 - (9) Sun, L.; Zheng, Q.; Li, N.; Chen, C.; Zhan, Z. Direct Electrolysis of CO₂ in Solid Oxide Cells Supported on Ceramic Fuel Electrodes with Straight Open Pores and Coated Catalysts. *Solid State Ion.* **2020**, *344*, 115154. <https://doi.org/10.1016/j.ssi.2019.115154>.
 - (10) Hjalmarsson, P.; Sun, X.; Liu, Y.-L.; Chen, M. Durability of High Performance Ni–Yttria Stabilized Zirconia Supported Solid Oxide Electrolysis Cells at High Current Density. *J. Power Sources* **2014**, *262*, 316–322. <https://doi.org/10.1016/j.jpowsour.2014.03.133>.
 - (11) Xu, S.; Li, S.; Yao, W.; Dong, D.; Xie, K. Direct Electrolysis of CO₂ Using an Oxygen-Ion Conducting Solid Oxide Electrolyzer Based on La_{0.75}Sr_{0.25}Cr_{0.5}Mn_{0.5}O_{3-δ} Electrode. *J. Power Sources* **2013**, *230*, 115–121. <https://doi.org/10.1016/j.jpowsour.2012.12.068>.
 - (12) Song, Y.; Zhou, Z.; Zhang, X.; Zhou, Y.; Gong, H.; Lv, H.; Liu, Q.; Wang, G.; Bao, X. Pure CO₂ Electrolysis over an Ni/YSZ Cathode in a Solid Oxide Electrolysis Cell. *J Mater Chem A* **2018**, *6* (28), 13661–13667. <https://doi.org/10.1039/C8TA02858C>.
 - (13) Li, X.; Wang, Y.; Liu, W.; Wilson, J. A.; Wang, J.; Wang, C.; Yang, J.; Xia, C.; Zhou, X.-D.; Guan, W. Reliability of CO₂ Electrolysis by Solid Oxide Electrolysis Cells with a Flat Tube Based on a Composite Double-Sided Air Electrode. *Compos. Part B Eng.* **2019**, *166*, 549–554.
<https://doi.org/10.1016/j.compositesb.2019.02.012>.
 - (14) Azucena Nepomuceno, M. C.; Kato, Y. Development of Disk-Type Solid Oxide Electrolysis Cell for CO₂ Reduction in an Active Carbon Recycling Energy System. *Energy Procedia* **2017**, *131*, 101–107. <https://doi.org/10.1016/j.egypro.2017.09.480>.
 - (15) Ahn, J.-Y.; Kim, B.-K.; Park, J.-S. Effects of Metal Catalysts on Co-Electrolysis of Steam and Carbon Dioxide. *J. Electrochem. Soc.* **2016**, *163* (10), F1288–F1293.
<https://doi.org/10.1149/2.1321610jes>.
 - (16) Fu, Q.; Mabilat, C.; Zahid, M.; Brisse, A.; Gautier, L. Syngas Production via High-Temperature Steam/CO₂ Co-Electrolysis: An Economic Assessment. *Energy Environ. Sci.* **2010**, *3* (10), 1382.
<https://doi.org/10.1039/c0ee00092b>.
 - (17) Ye, L.; Zhang, M.; Huang, P.; Guo, G.; Hong, M.; Li, C.; Irvine, J. T. S.; Xie, K. Enhancing CO₂ Electrolysis through Synergistic Control of Non-Stoichiometry and Doping to Tune Cathode Surface Structures. *Nat. Commun.* **2017**, *8*, 1–10. <https://doi.org/10.1038/ncomms14785>.
 - (18) Ebbesen, S. D.; Knibbe, R.; Mogensen, M. Co-Electrolysis of Steam and Carbon Dioxide in Solid Oxide Cells. *J. Electrochem. Soc.* **2012**, *159* (8), F482–F489.
<https://doi.org/10.1149/2.076208jes>.
 - (19) Wang, Y.; Liu, T.; Fang, S.; Chen, F. Syngas Production on a Symmetrical Solid Oxide H₂O/CO₂ Co-Electrolysis Cell with Sr₂Fe_{1.5}Mo_{0.5}O₆–Sm_{0.2}Ce_{0.8}O_{1.9} Electrodes. *J. Power Sources* **2016**, *305*, 240–248. <https://doi.org/10.1016/j.jpowsour.2015.11.097>.
 - (20) Xu, J.; Zhou, X.; Cheng, J.; Pan, L.; Wu, M.; Dong, X.; Sun, K. Electrochemical Performance of Highly Active Ceramic Symmetrical Electrode La_{0.3}Sr_{0.7}Ti_{0.3}Fe_{0.7}O_{3-δ}-CeO₂ for Reversible Solid Oxide Cells. *Electrochimica Acta* **2017**, *257*, 64–72.
<https://doi.org/10.1016/j.electacta.2017.10.061>.

- (21) Yue, X.; Irvine, J. T. S. (La,Sr)(Cr,Mn)O₃/GDC Cathode for High Temperature Steam Electrolysis and Steam-Carbon Dioxide Co-Electrolysis. *Solid State Ion.* **2012**, *225*, 131–135. <https://doi.org/10.1016/j.ssi.2012.06.015>.
- (22) Lillmaa, K.; Maide, M.; Kanarbik, R.; Nurk, G.; Lust, E. Electrochemical Characteristics and Gas Composition Generated by La_{0.8}Sr_{0.2}Cr_{0.5}Mn_{0.5}O_{3-δ} Cathode at Electrolysis and Co-Electrolysis Modes. *J. Electrochem. Soc.* **2016**, *163* (11), F3190–F3196. <https://doi.org/10.1149/2.0261611jes>.
- (23) Yoon, S.-E.; Song, S.-H.; Choi, J.; Ahn, J.-Y.; Kim, B.-K.; Park, J.-S. Coelectrolysis of Steam and CO₂ in a Solid Oxide Electrolysis Cell with Ceramic Composite Electrodes. *Int. J. Hydrog. Energy* **2014**, *39* (11), 5497–5504. <https://doi.org/10.1016/j.ijhydene.2014.01.124>.
- (24) Yoon, S.-E.; Ahn, J.-Y.; Kim, B.-K.; Park, J.-S. Improvements in Co-Electrolysis Performance and Long-Term Stability of Solid Oxide Electrolysis Cells Based on Ceramic Composite Cathodes. *Int. J. Hydrog. Energy* **2015**, *40* (39), 13558–13565. <https://doi.org/10.1016/j.ijhydene.2015.08.012>.
- (25) Addo, P. K.; Molero-Sanchez, B.; Chen, M.; Paulson, S.; Birss, V. CO/CO₂ Study of High Performance La_{0.3}Sr_{0.7}Fe_{0.7}Cr_{0.3}O_{3-δ} Reversible SOFC Electrodes. *Fuel Cells* **2015**, *15* (5), 689–696. <https://doi.org/10.1002/face.201400196>.
- (26) Li, Y.; Li, P.; Hu, B.; Xia, C. A Nanostructured Ceramic Fuel Electrode for Efficient CO₂/H₂O Electrolysis without Safe Gas. *J Mater Chem A* **2016**, *4* (23), 9236–9243. <https://doi.org/10.1039/C6TA02830F>.
- (27) Wang, W.; Gan, L.; Lemmon, J. P.; Chen, F.; Irvine, J. T. S.; Xie, K. Enhanced Carbon Dioxide Electrolysis at Redox Manipulated Interfaces. *Nat. Commun.* **2019**, *10* (1), 1–10. <https://doi.org/10.1038/s41467-019-09568-1>.
- (28) Yu, Y.; Mao, B.; Geller, A.; Chang, R.; Gaskell, K.; Liu, Z.; Eichhorn, B. W. CO₂ Activation and Carbonate Intermediates: An Operando AP-XPS Study of CO₂ Electrolysis Reactions on Solid Oxide Electrochemical Cells. *Phys Chem Chem Phys* **2014**, *16* (23), 11633–11639. <https://doi.org/10.1039/C4CP01054J>.
- (29) Chen, M.; Liu, Y.-L.; Bentzen, J. J.; Zhang, W.; Sun, X.; Hauch, A.; Tao, Y.; Bowen, J. R.; Hendriksen, P. V. Microstructural Degradation of Ni/YSZ Electrodes in Solid Oxide Electrolysis Cells under High Current. *J. Electrochem. Soc.* **2013**, *160* (8), F883–F891. <https://doi.org/10.1149/2.098308jes>.
- (30) Tao, Y.; Ebbesen, S. D.; Mogensen, M. B. Degradation of Solid Oxide Cells during Co-Electrolysis of Steam and Carbon Dioxide at High Current Densities. *J. Power Sources* **2016**, *328*, 452–462. <https://doi.org/10.1016/j.jpowsour.2016.08.055>.
- (31) Knibbe, R.; Traulsen, M. L.; Hauch, A.; Ebbesen, S. D.; Mogensen, M. Solid Oxide Electrolysis Cells: Degradation at High Current Densities. *J. Electrochem. Soc.* **2010**, *157* (8), B1209. <https://doi.org/10.1149/1.3447752>.
- (32) Hanifi, A. R.; Laguna-Bercero, M. A.; Sandhu, N. K.; Etsell, T. H.; Sarkar, P. Tailoring the Microstructure of a Solid Oxide Fuel Cell Anode Support by Calcination and Milling of YSZ. *Sci. Rep.* **2016**, *6* (1), 27359. <https://doi.org/10.1038/srep27359>.
- (33) Cheng, Z.; Wang, J.-H.; Choi, Y.; Yang, L.; Lin, M. C.; Liu, M. From Ni-YSZ to Sulfur-Tolerant Anode Materials for SOFCs: Electrochemical Behavior, in Situ Characterization, Modeling, and Future Perspectives. *Energy Environ. Sci.* **2011**, *4* (11), 4380. <https://doi.org/10.1039/c1ee01758f>.
- (34) Dong, D.; Xu, S.; Shao, X.; Hucker, L.; Marin, J.; Pham, T.; Xie, K.; Ye, Z.; Yang, P.; Yu, L.; Parkinson, G.; Li, C.-Z. Hierarchically Ordered Porous Ni-Based Cathode-Supported Solid Oxide Electrolysis Cells for Stable CO₂ Electrolysis without Safe Gas. *J. Mater. Chem. A* **2017**, *5* (46), 24098–24102. <https://doi.org/10.1039/C7TA06839E>.
- (35) Song, Y.; Zhou, Z.; Zhang, X.; Zhou, Y.; Gong, H.; Lv, H.; Liu, Q.; Wang, G.; Bao, X. Pure CO₂ Electrolysis over an Ni/YSZ Cathode in a Solid Oxide Electrolysis Cell. *J. Mater. Chem. A* **2018**, *6* (28), 13661–13667. <https://doi.org/10.1039/C8TA02858C>.

- (36) Yan, J.; Chen, H.; Dogdibegovic, E.; Stevenson, J. W.; Cheng, M.; Zhou, X.-D. High-Efficiency Intermediate Temperature Solid Oxide Electrolyzer Cells for the Conversion of Carbon Dioxide to Fuels. *J. Power Sources* **2014**, *252*, 79–84. <https://doi.org/10.1016/j.jpowsour.2013.11.047>.
- (37) Bidrawn, F.; Kim, G.; Corre, G.; Irvine, J. T. S.; Vohs, J. M.; Gorte, R. J. Efficient Reduction of CO₂ in a Solid Oxide Electrolyzer. *Electrochem. Solid-State Lett.* **2008**, *11* (9). <https://doi.org/10.1149/1.2943664>.
- (38) Toebes, M. Impact of the Structure and Reactivity of Nickel Particles on the Catalytic Growth of Carbon Nanofibers. *Catal. Today* **2002**, *76* (1), 33–42. [https://doi.org/10.1016/S0920-5861\(02\)00209-2](https://doi.org/10.1016/S0920-5861(02)00209-2).
- (39) Whipple, D. T.; Kenis, P. J. A. Prospects of CO₂ Utilization via Direct Heterogeneous Electrochemical Reduction. *J. Phys. Chem. Lett.* **2010**, *1* (24), 3451–3458. <https://doi.org/10.1021/jz1012627>.
- (40) Kim, S. W.; Park, M.; Kim, H.; Yoon, K. J.; Son, J. W.; Lee, J. H.; Kim, B. K.; Lee, J. H.; Hong, J. In-Situ Nano-Alloying Pd-Ni for Economical Control of Syngas Production from High-Temperature Thermo-Electrochemical Reduction of Steam/CO₂. *Appl. Catal. B Environ.* **2017**, *200*, 265–273. <https://doi.org/10.1016/j.apcatb.2016.07.008>.
- (41) Choi, S.; Sang, B. I.; Hong, J.; Yoon, K. J.; Son, J. W.; Lee, J. H.; Kim, B. K.; Kim, H. Catalytic Behavior of Metal Catalysts in High-Temperature RWGS Reaction: In-Situ FT-IR Experiments and First-Principles Calculations. *Sci. Rep.* **2017**, *7* (May 2016), 1–10. <https://doi.org/10.1038/srep41207>.
- (42) Hu, X.; Xie, K. Active and Stable Ni/Cr₂O₃- δ Cathodes for High Temperature CO₂ Electrolysis. *J. Power Sources* **2019**, *430*, 20–24. <https://doi.org/10.1016/j.jpowsour.2019.05.014>.
- (43) Ye, L.; Hu, X.; Wang, X.; Chen, F.; Tang, D.; Dong, D.; Xie, K. Enhanced CO₂ Electrolysis with a SrTiO₃ Cathode through a Dual Doping Strategy. *J. Mater. Chem. A* **2019**, *7* (6), 2764–2772. <https://doi.org/10.1039/c8ta10188d>.
- (44) Wang, W.; Gan, L.; Lemmon, J. P.; Chen, F.; Irvine, J. T. S.; Xie, K. Enhanced Carbon Dioxide Electrolysis at Redox Manipulated Interfaces. *Nat. Commun.* **2019**, *10* (1), 1550. <https://doi.org/10.1038/s41467-019-09568-1>.
- (45) Rutman, J.; Riess, I. Placement of Reference Electrode in Solid State Electrolyte Cells. *Solid State Ion.* **2008**, *179* (21–26), 913–918. <https://doi.org/10.1016/j.ssi.2008.01.071>.
- (46) Kim, J. H.; Yoo, S.; Murphy, R.; Chen, Y.; Ding, Y.; Pei, K.; Zhao, B.; Kim, G.; Choi, Y.; Liu, M. Promotion of Oxygen Reduction Reaction on a Double Perovskite Electrode by a Water-Induced Surface Modification. *Energy Environ. Sci.* **2021**, *14* (3), 1506–1516. <https://doi.org/10.1039/D0EE03283B>.
- (47) Naumenko, A.; Berezovska, N.; Biliy, M.; Shevchenko, O. V. Vibrational Analysis and Raman Spectra of Tetragonal Zirconia. *Phys Chem Solid State* **2008**, *9*, 121–125.
- (48) Mironova-Ulmane, N.; Kuzmin, A.; Sildos, I.; Puust, L.; Grabis, J. Magnon and Phonon Excitations in Nanosized NiO. *Latv. J. Phys. Tech. Sci.* **2019**, *56* (2), 61–72. <https://doi.org/10.2478/lpts-2019-0014>.
- (49) Yang, X.; Liu, W.; Pan, G.; Sun, Y. Modulation of Oxygen in NiO:Cu Films toward a Physical Insight of NiO:Cu/c-Si Heterojunction Solar Cells. *J. Mater. Sci.* **2018**, *53* (16), 11684–11693. <https://doi.org/10.1007/s10853-018-2430-1>.
- (50) Yadav, V. K.; Shinde, H. P.; Das, T. Oxidation of Cyclohexane Using Copper–Nickel Catalyst. *Arab. J. Sci. Eng.* **2021**. <https://doi.org/10.1007/s13369-021-05547-1>.
- (51) Liaqat, R.; Mansoor, M. A.; Iqbal, J.; Jilani, A.; Shakir, S.; Kalam, A.; Wageh, S. Fabrication of Metal (Cu and Cr) Incorporated Nickel Oxide Films for Electrochemical Oxidation of Methanol. *Crystals* **2021**, *11* (11). <https://doi.org/10.3390/cryst11111398>.
- (52) Murthy, P. S.; Venugopalan, V. P.; Das, D. A.; Dhara, S.; Pandiyan, R.; Tyagi, A. K. Antibiofilm Activity of Nano Sized CuO. In *International Conference on Nanoscience, Engineering and Technology (ICONSET 2011)*; IEEE: Chennai, 2011; pp 580–583. <https://doi.org/10.1109/ICONSET.2011.6168037>.

- (53) Lacerda, M. M.; Kargar, F.; Aytan, E.; Samnakay, R.; Debnath, B.; Li, J. X.; Khitun, A.; Lake, R. K.; Shi, J.; Balandin, A. A. Variable-Temperature Inelastic Light Scattering Spectroscopy of Nickel Oxide: Disentangling Phonons and Magnons. *Appl. Phys. Lett.* **2017**, *110* (20), 202406. <https://doi.org/10.1063/1.4983810>.
- (54) Lucazeau, G. Effect of Pressure and Temperature on Raman Spectra of Solids: Anharmonicity. *J. Raman Spectrosc.* **2003**, *34* (7–8), 478–496. <https://doi.org/10.1002/jrs.1027>.
- (55) Chen, Y.; Choi, Y.; Yoo, S.; Ding, Y.; Yan, R.; Pei, K.; Qu, C.; Zhang, L.; Chang, I.; Zhao, B.; Zhang, Y.; Chen, H.; Chen, Y.; Yang, C.; deGlee, B.; Murphy, R.; Liu, J.; Liu, M. A Highly Efficient Multi-Phase Catalyst Dramatically Enhances the Rate of Oxygen Reduction. *Joule* **2018**, *2* (5), 938–949. <https://doi.org/10.1016/j.joule.2018.02.008>.
- (56) Kim, J. H.; Yoo, S.; Murphy, R.; Chen, Y.; Ding, Y.; Pei, K.; Zhao, B.; Kim, G.; Choi, Y.; Liu, M. Promotion of Oxygen Reduction Reaction on a Double Perovskite Electrode by a Water-Induced Surface Modification. *Energy Environ. Sci.* **2021**. <https://doi.org/10.1039/d0ee03283b>.
- (57) Yang, Y.; Li, Y.; Jiang, Y.; Zheng, M.; Hong, T.; Wu, X.; Xia, C. The Electrochemical Performance and CO₂ Reduction Mechanism on Strontium Doped Lanthanum Ferrite Fuel Electrode in Solid Oxide Electrolysis Cell. *Electrochimica Acta* **2018**, *284*, 159–167. <https://doi.org/10.1016/j.electacta.2018.07.187>.
- (58) Feng, Z. A.; Machala, M. L.; Chueh, W. C. Surface Electrochemistry of CO₂ Reduction and CO Oxidation on Sm-Doped CeO_{2-x}: Coupling between Ce³⁺ and Carbonate Adsorbates. *Phys Chem Chem Phys* **2015**, *17* (18), 12273–12281. <https://doi.org/10.1039/C5CP00114E>.
- (59) Opitz, A. K.; Nanning, A.; Rameshan, C.; Kubicek, M.; Götsch, T.; Blume, R.; Hävecker, M.; Knop-Gericke, A.; Rupprechter, G.; Klötzer, B.; Fleig, J. Surface Chemistry of Perovskite-Type Electrodes during High Temperature CO₂ Electrolysis Investigated by Operando Photoelectron Spectroscopy. *ACS Appl. Mater. Interfaces* **2017**, *9* (41), 35847–35860. <https://doi.org/10.1021/acsami.7b10673>.
- (60) Albrecht, P. M.; Jiang, D.; Mullins, D. R. CO₂ Adsorption As a Flat-Lying, Tridentate Carbonate on CeO₂(100). *J. Phys. Chem. C* **2014**, *118* (17), 9042–9050. <https://doi.org/10.1021/jp501201b>.
- (61) Zhou, Y.; Martín, A. J.; Dattila, F.; Xi, S.; López, N.; Pérez-Ramírez, J.; Yeo, B. S. Long-Chain Hydrocarbons by CO₂ Electroreduction Using Polarized Nickel Catalysts. *Nat. Catal.* **2022**, *5* (6), 545–554. <https://doi.org/10.1038/s41929-022-00803-5>.